Int. J. Electrochem. Sci., 15 **(2020)** 1571 – 1580, doi: 10.20964/2020.02.43

International Journal of
ELECTROCHEMICAL
SCIENCE
www.electrochemsci.org

The Effect of Calcination Temperature on Combustion Preparation of $ZnFe_2O_4$ as Anode for Lithium Batteries

Jiaming Liu[1], *Yanhua Lu*[1], *Ruixiang Wang*[1], *Zhifeng Xu*[1,*], *Xue Li*[2,*]

[1] School of Metallurgy Engineering, Jiangxi University of Science and Technology, Ganzhou 341000, PR China
[2] National and Local Joint Engineering Laboratory for Lithium-ion Batteries and Materials Preparation Technology, Key Laboratory of Advanced Battery Materials of Yunnan Province, Faculty of Metallurgical and Energy Engineering, Kunming University of Science and Technology, Kunming 650093, PR China
[*]E-mail: xu.zf@jxust.edu.cn, 438616074@qq.com

Received: 7 October 2019 / *Accepted:* 29 November 2019 / *Published:* 31 December 2019

A porous structure of $ZnFe_2O_4$ was prepared by combustion. The effects of the self-propagation reaction and calcination temperature on the morphological and electrochemical energy storage properties of $ZnFe_2O_4$ were studied. The results show that with the combustion reaction of the dry gel at 169.8 °C, the crystallinity and grain size of the pure phase $ZnFe_2O_4$ are positively correlated with the increase of calcination temperature. Due to its highly porous structure and good crystallinity, the calcined $ZnFe_2O_4$ at 700 °C shows the best electrochemical performance. The first specific discharge capacity reaches 1482.4 mAh g^{-1}, and the reversible capacity after 50 cycles is still 1319.4 mAh g^{-1}. The rate performance test indicates that the 700 °C sample has a very good reversible capacity and an excellent rate performance over a wide current density range. At a high current rate of 1600 mA g^{-1}, the reversible capacity can be kept above 900 mAh g^{-1}. The above results indicate that the combustion method is indeed a simple and efficient method for preparing ferrite, and the obtained material has good electrochemical properties.

Keywords: $ZnFe_2O_4$, combustion preparation, lithium batteries, anode materials

1. INTRODUCTION

Lithium-ion batteries (LIBs) play an increasingly important role in people's daily life[1-3]. Graphite, as the main anode material for lithium-ion batteries, has a theoretical specific capacity of only 372 mAh g^{-1}; however, it is difficult to meet the market demand for high-energy-density lithium-ion batteries[4-7]. Therefore, it is important to develop a new generation of anode materials for lithium-ion batteries with a high energy density and high cycle stability. Transition metallic oxides have become a

research hotspot due to their ultrahigh specific capacity and unique conversion lithium storage mechanism[8,9]. They are strong candidates for being the next generation of lithium-ion battery anode materials. Binary metallic oxides such as zinc ferrite ($ZnFe_2O_4$) have the following advantages over single metal oxides[10,11]. (1) The volume expansion coefficients of Zn and Fe are different, which can be coordinated with each other during charge and discharge and further alleviates the volume expansion of the material. (2) The electron transfer activation energy between the metal elements is lower and they have a higher electron conductivity in comparison to those of some metal oxides in a single phase. These advantages make ferrite an excellent negative electrode material. Due to the dramatic volume change of the metal oxide lithium storage process, the electrochemical properties of the materials are closely related to the particle morphology and microstructure. Controlling the preparation method and process conditions can have a critical impact on the morphology and structure of the material[12]. Traditional methods for the preparation of ferrite such as solid phase calcination at high temperature[13], hydrothermal preparation[14], coprecipitation preparation[15] and template preparation[16], have in long reaction processes, complicated procedures and extensive equipment requirements. Furthermore, the organic salts, active agents or templates used in the above experiments can cause environmental pollution.

In response to the above problems, this paper introduces a combustion method that is energy efficient and simple to conduct. The process of preparing $ZnFe_2O_4$ by the combustion method saves time and provides a uniform distribution of the metal elements. After heat treatment, as shown in the XRD data, the crystallinity of the material is high without any impurity phase. The obtained 700 °C-$ZnFe_2O_4$ exhibits good energy storage performance, and the capacity reaches 1319.4 mAh g^{-1} after 50 cycles.

2. EXPERIMENTAL

2.1 Materials preparation

The preparation process of $ZnFe_2O_4$ by the combustion method is as follows. A stoichiometric ratio of zinc nitrate ($Zn(NO_3)_2 \cdot 6H_2O$) and ferric nitrate ($Fe(NO_3)_3 \cdot 9H_2O$) were mixed and dissolved in deionized water and then added to the mixed solution. A certain proportion of glycine ($C_2H_5NO_2$) acted as a complexing agent and a flammable agent. After the solution was completely dissolved, the beaker was placed in a 90 °C oil bath and heated until the water was evaporated to dryness, and the solute formed a dry gel. The dried gel was removed and placed in a crucible, where it was heated and ignited in an electric furnace. The dry gel underwent a creep reaction to form a precursor. The crucible containing the precursor was placed in a muffle furnace and calcined at 600 °C, 700 °C, and 800 °C for 2 h in an air atmosphere. After heating, the muffle furnace was naturally cooled, and the final product was obtained.

2.2 Characterization

Phase analysis was performed using a Japanese Neoclassical MiniFlex 600 X-ray diffractometer (XRD, Cu target, λ = 1.5405 Å). The morphology and structure of the sample were observed by a

VEGA3 SBU/SBH scanning electron microscope (SEM) and a JEM-2100 transmission electron microscope (TEM). The dry gel pyrolysis process was studied using a NETZSCH STA 449F3 synchronous thermal analyzer.

2.3 Electrochemical test

The obtained active material $ZnFe_2O_4$, conductive agent (super P) and polyvinylidene fluoride (PVDF) were mixed in a certain amount of N-methylpyrrolidone (NMP) according to a mass ratio of 7:2:1 and stirred into a slurry by magnetic stirring. The slurry was evenly spread on a copper foil by a coater and dried under vacuum at 120 °C for 10 h. The electrode film was rolled and sliced and used as a working electrode. A lithium metal plate was used as the counter electrode, and 1 $mol \cdot L^{-1}$ of $LiPF_6$ (dissolved in a volume ratio of 1:1:1 EC/DMC/DEC) was used as the electrolyte. The assembly of a CR2016 coin battery was carried out in a full argon glove box. The assembled battery was tested by a Wuhan Blue Battery Test System for charge and discharge performance, and the cyclic voltammetry curve was tested with Metrohm Autolab PGSTAT302N.

3. RESULTS AND DISCUSSION

To study the dry gel self-propagation reaction process, the dry gel was subjected to thermogravimetry-differential thermal analysis. Figure 1 shows the residual weight change and endothermic/exothermic process of the xerogel from room temperature to 800 °C. The TG curve of the sample has a significant drop in the initial stage, corresponding to the gradual evaporation of water in the dry gel.

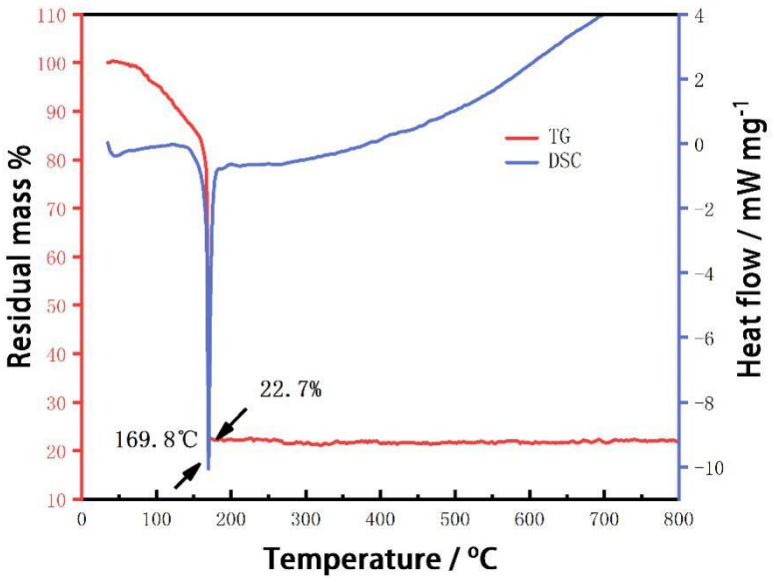

Figure 1. Thermogravimetry curve of the $ZnFe_2O_4$ xerogel.

The sample has only one exothermic peak, located at approximately 169.8 °C, which represents the self-propagation reaction of the xerogel. This exothermic peak is very sharp, and the related reaction releases a heat flux of approximately 10.32 mW mg^{-1} for a short duration. The TG curve corresponding to this exothermic peak indicates a huge weight loss step. During the combustion reaction, nitrogen and carbon in the xerogel are converted into gas and quickly escape. Finally, the dry gel remains 22.7% by weight in the form of oxide.

Figure 2 is a partially enlarged view of the XRD pattern and a (311) peak of $ZnFe_2O_4$ is obtained at different calcination temperatures. Figure. 2(a) shows that the characteristic peak positions of the three groups of samples are completely consistent with the standard PDF (PDF Card, No. 22-1012) card of a spinel-type $ZnFe_2O_4$. As the temperature for the heat treatment increases, the sharpness of the characteristic peak of the sample also gradually increases, which means that the sample has the best crystallinity at a high calcination temperature. From Fig. 2(b), it can be found that the (311) peak has a tendency to split at high heat treatment temperatures, which may be due to the decomposition of $ZnFe_2O_4$ caused by the excessive heat treatment temperature or the formation of a new phase[17]. The unit cell parameters and average grain size of the sample were calculated using the Scherrer formula (Table 1). The average grain sizes of $ZnFe_2O_4$ at 600 °C, 700 °C and 800 °C are 85, 91 and 116 nm, respectively, and the unit cell parameters rise gradually with increasing heat treatment temperature[17].

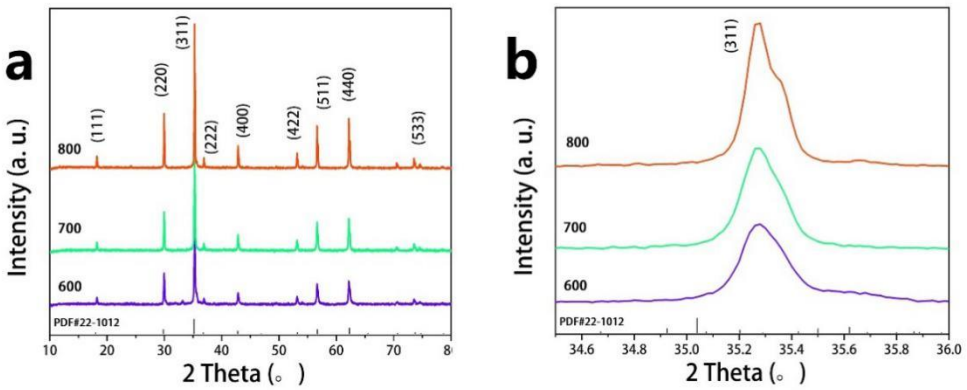

Figure 2. XRD patterns of $ZnFe_2O_4$ after calcination and the partial enlargement of (311) peak.

Table 1. Unit cell parameters and average grain sizes of $ZnFe_2O_4$ after calcination.

	Cell parameters			Average particle size (nm)
	a (Å)	b (Å)	c (Å)	
600℃	8.4337 (5)	8.4337 (5)	8.4337 (5)	85
700℃	8.4365 (5)	8.4365 (5)	8.4365 (5)	91
800℃	8.4484 (5)	8.4484 (5)	8.4484 (5)	116

Figure 3 shows SEM images of the obtained $ZnFe_2O_4$ and a TEM image of the 700 °C sample. From the figure, it can be seen that the prepared samples all have a pore structure; the number of pores

in the 700 °C sample is relatively abundant, whereas the sample at 800 °C has fewer pores, but they are smoother and larger. The pores increase the specific surface area of the material and facilitate the contact of the material with the electrolyte. In addition, the pores can also alleviate the volume change of the lithium storage process, which avoids material pulverization, protects the electrode structure, and thus, extends battery life. From Fig. 3(d), it can be further determined that the grain size distribution is between 75 and 105 nm.

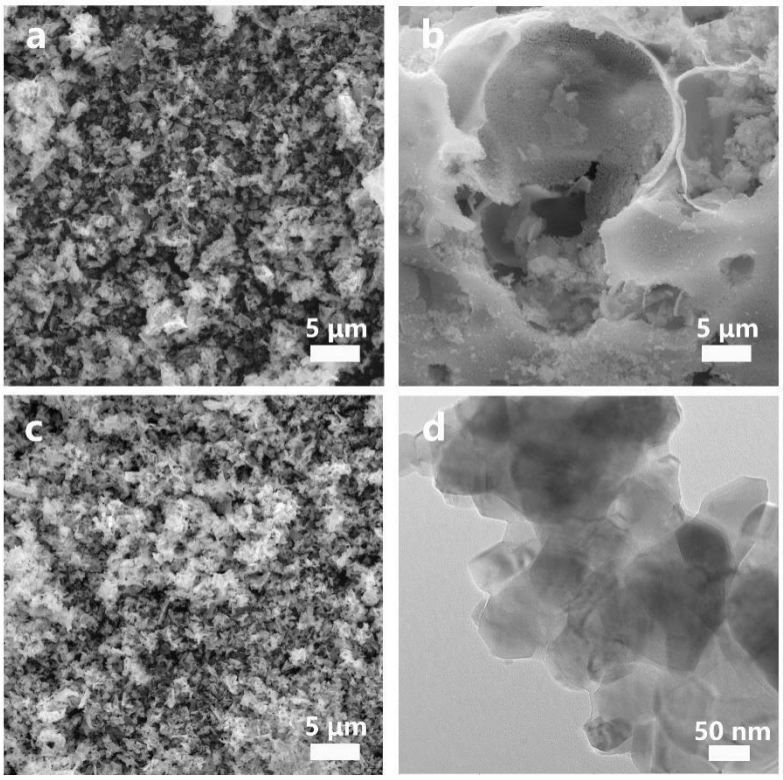

Figure 3. a-c SEM images of $ZnFe_2O_4$ after calcination and **d** a TEM image of 700 ℃ sample.

A cyclic voltammetry test of $ZnFe_2O_4$ can be used to observe the oxidation-reduction potential of the electrode charge-discharge reaction and help to understand the reaction mechanism of the material in the process of lithium deintercalation. Figure 4 is a cyclic voltammetry graph of a $ZnFe_2O_4$ electrode after calcination at 700 °C. As shown in the figure, the redox peak of the first cycle is significantly different from those of the last two cycles, indicating that there is a different lithium storage reaction mechanism. During the first discharge, $ZnFe_2O_4$ reacts with Li^+ to form $Li_{0.5}ZnFe_2O_4$ (Reaction 1), after which $Li_2ZnFe_2O_4$ is further formed (Reaction 2). A sharp reduction peak was observed at 0.71 V, corresponding to $Li_2MFe_2O_4$ consuming 6 lithium ions and producing metallic Zn and Fe and amorphous Li_2O (Reaction 3). Zn can also be alloyed with Li^+ to form Zn-Li (Reaction 4). In the second cycle, the reduction peak was shifted to 0.98 V (Reaction 5) due to the rearrangement of the material structure and the reduction of the transition metal element (Reaction 6)[18]. The oxidation peak of the first ring is located near 1.68 V, which corresponds to the oxidation of Zn and Fe to ZnO and Fe_2O_3, respectively.

The oxide peak stacking at approximately 1.74 V in the last two cycles indicates that the material has good electrochemical reversibility without an obvious polarization phenomenon.

$$ZnFe_2O_4 + 0.5Li^+ + 0.5e^- \leftrightarrow Li_{0.5}ZnFe_2O_4 \quad (1)$$

$$Li_{0.5}ZnFe_2O_4 + 1.5Li^+ + 1.5e^- \leftrightarrow Li_2ZnFe_2O_4 \quad (2)$$

$$Li_2ZnFe_2O_4 + 6Li^+ + 6e^- \rightarrow Li_2O + Zn + 2Fe \quad (3)$$

$$Zn + Li^+ + e^- \leftrightarrow Zn\text{-}Li \quad (4)$$

$$3Li_2O + 2Fe \leftrightarrow Fe_2O_3 + 6Li^+ + 6e^- \quad (5)$$

$$Li_2O + Zn \leftrightarrow ZnO + 2Li^+ + 2e^- \quad (6)$$

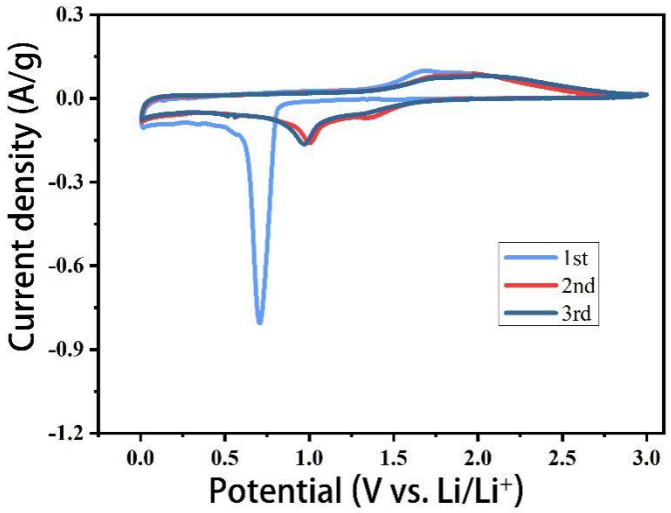

Figure 4. Cyclic voltammetry curves of the 700 °C-$ZnFe_2O_4$ electrode with a scanning rate of 0.2 mV s^{-1} in a scanning range of 0.01 ~ 3.0 V (vs. Li/Li^+).

Figure 5 and Table 2 show the charge and discharge cycles of three groups of $ZnFe_2O_4$ at a current density of 200 mA g^{-1} for 50 cycles. The coulombic efficiencies of the samples are similar; the first coulombic efficiency is above 70% and then above 98% in the next cycle. The low first coulombic efficiency results from the formation of an SEI film on the electrode surface, leading to the deterioration and recombination of the material structure, thus, some of the capacity is irreversible[19]. The comparison shows that the charge and discharge capacity of the sample shows an upward trend, in which the curve of the 700 °C-sample rises relatively steeply with obvious capacity increases, and the curves of the 600 °C-sample and 800 °C-sample are relatively flat. The increase in capacity is due to the presence of a polymeric gel-like film on the surface of the electrode. This film results from the decomposition of the electrolyte and the accompanying kinetic activation, resulting in the appearance of a pseudocapacitor effect and thus increased Li^+ storage[20,21]. The 700 °C-sample has the highest initial capacity, reaching 1119.2/1482.4 mAh g^{-1}, and the specific capacity after 50 cycles reaches 1310.7/1319.4 mAh g^{-1}, which is still the highest out of the three tested groups. There is a downward trend after 50 cycles for the 800 °C-sample, but the capacity can still reach 984/995.1 mAh g^{-1}, which may be due to the agglomeration effect of small particles at high temperature. At the same time, some

of the pores disappear, and the specific surface area decreases. From the above data, it can be found that the charge and discharge capacity of the 700 °C-sample is retained at a high level, and the advantage is remarkable when compared with those of the other temperature samples.

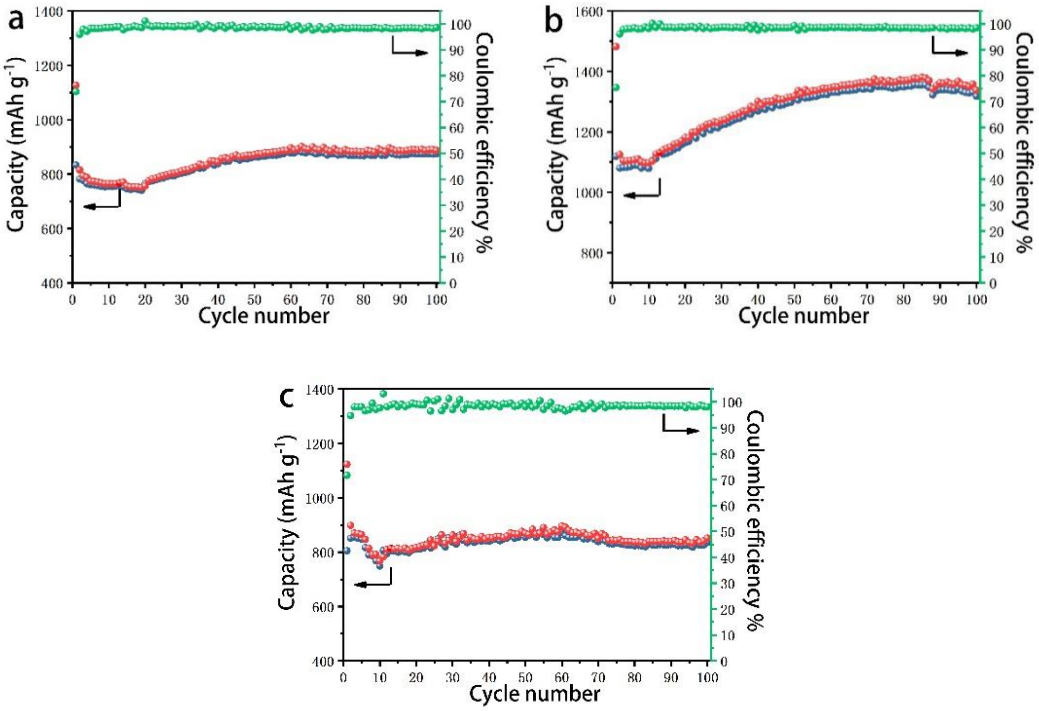

Figure 5. Charge and discharge cycling curves of **a** 600 °C-$ZnFe_2O_4$, **b** 700 °C-$ZnFe_2O_4$, and **c** 800 °C-$ZnFe_2O_4$.

Table 2. Comparison of the electrochemical performance of the prepared $ZnFe_2O_4$ samples.

Sample	1st cycle charge/discharge capacity (mAh g^{-1})	50th cycle charge/discharge capacity (mAh g^{-1})	100th cycle charge/discharge capacity (mAh g^{-1})
600℃	943/1264.3	1062.4/1083.2	874.3/887
700℃	1119.2/1482.4	1310.7/1319.4	1317.7/1338
800℃	962.4/1269.5	984/995.1	835.6/851.7

In order to understand the rate performance of the material, three groups of samples were tested at different current densities, such as 100, 200, 400, 800, 1600 mA g^{-1}. As shown in Figure 6, capacity reduction trend occurs in each group of samples at the initial stage. This may be due to the formation of SEI film on the surface of the electrode, resulting in deterioration of the material structure and recombination. At each subsequent cycling, the 700 ℃ sample shows a significant specific capacity advantage and an upward trend, indicating that the lithium storage capacity is gradually increased under the effect of the pseudocapacitor effect. The 600 ℃ and 800 ℃ show a relatively stable cycling performance. In the final small current density charge and discharge phase, the average specific

discharge capacity of the 700 ℃ sample can still be maintained at 1228.5 mAh g^{-1}, while the average discharge specific capacity of the sample at 600 ℃ and 800 ℃ is only 845.7 and 999.1 mAh g^{-1}. The rate performance test indicates that the 700 ℃ sample has a very good capacity reversibility and excellent rate performance over a wide current density range. The outstanding cycling stability characteristics of the porous $ZnFe_2O_4$ electrode are summarized in Table 3 that also compares them with the cycling stability characteristics previously reported for other ferrites used as anodes for Lithium-ion battery and Sodium-ion batteries systems.

To understand the rate performance of the material, three groups of samples were tested at different current densities, such as 100, 200, 400, 800, and 1600 mA g^{-1}. As shown in Figure 6, a trend of decreasing capacity occurs in each group of samples at the initial stage. This may be due to the formation of the SEI film on the surface of the electrode, resulting in the deterioration of the material structure and its recombination. At each subsequent cycling, the 700 °C sample shows a significant specific capacity advantage and an upward trend, indicating that the lithium storage capacity is gradually increased under the effect of the pseudocapacitor effect. The 600 °C and 800 °C show a relatively stable cycling performance. In the final small current density charge and discharge phase, the average specific discharge capacity of the 700 °C sample can still be kept at 1228.5 mAh g^{-1}, while the average discharge specific capacity of the sample at 600 °C and 800 °C is only 845.7 and 999.1 mAh g^{-1}, respectively. The rate performance test indicates that the 700 °C sample has a very good reversible capacity and excellent rate performance over a wide current density range. The outstanding cycling stability characteristics of the porous $ZnFe_2O_4$ electrodes are summarized in Table 3, which also compares them with the cycling stability characteristics previously reported for other ferrites used as anodes in lithium-ion battery and sodium-ion battery systems.

Table 3. Comparison of the results in this study with reported performance of other ferrite materials used as LIB and SIB anodes.

Sample	Cyclic stability	Reference
Porous $ZnFe_2O_4$	1338 mAh g^{-1} at 200 mA g^{-1} (100 cycles)	Present work
(LIBs) Nanostructured $MgFe_2O_4$	300 mAh g^{-1} at 0.2 mA cm^{-2} (100 cycles)	[22]
(LIBs) $MgFe_2O_4$ nanoparticles	493 mAh g^{-1} at 90 mA g^{-1} (50 cycles)	[23]
(LIBs) Cubic $CoFe_2O_4$ nanoparticle	1133.5 mAh g^{-1} at 100 mA g^{-1} (120 cycles)	[24]
(LIBs) $CuFe_2O_4$ nanotubes	816 mAh g^{-1} at 200 mA g^{-1} (50 cycles)	[25]
(LIBs) $ZnFe_2O_4$ microcages	824 mAh g^{-1} at 200 mA g^{-1} (100 cycles)	[26]
(SIBs) Rod-like $CuFe_2O_4$	281 mAh g^{-1} at 100 mA g^{-1} (20 cycles)	[27]
(SIBs) $MnFe_2O_4$/rGO composites	347.5 mAh g^{-1} at 50 mA g^{-1} (70 cycles)	[28]
(SIBs) $MnFe_2O_4$/rGO nanocomposite	258 mAh g^{-1} at 92.8 mA g^{-1} (50 cycles)	[29]

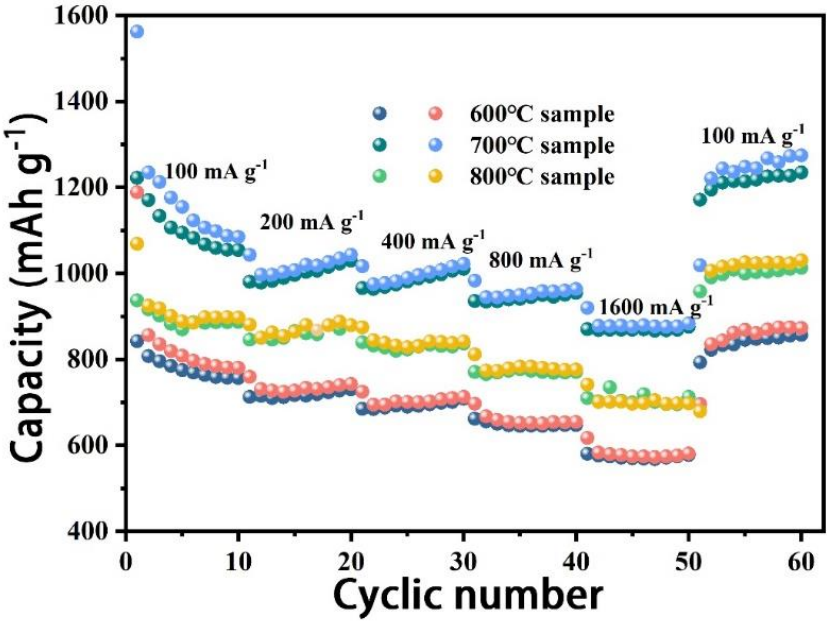

Figure 6. Rate performance of **a** 600 °C-$ZnFe_2O_4$, **b** 700 °C-$ZnFe_2O_4$, and **c** 800 °C-$ZnFe_2O_4$.

4. CONCLUSION

In this paper, a spinel-type $ZnFe_2O_4$ lithium ion anode material was successfully prepared by combustion, and the effects of different calcination temperatures on the morphology and electrochemical properties of the $ZnFe_2O_4$ phase were studied in detail. The XRD and SEM results show that the obtained sample has good crystallinity without impurities, and the grain size gradually increases with increasing calcination temperature. The grain size of the sample at 700 °C is approximately 91 nm, and the surface of the particle has an abundance of pores. In the electrochemical test, the 700 °C-sample shows significantly better electrochemical performance than that of the 600 °C-sample and 800 °C-sample, and the specific discharge capacity after 50 cycles reaches 1319.4 mAh g^{-1}. The 700 °C-sample also has a better rate performance; at a high current rate of 1600 mA g^{-1}, the reversible capacity can be kept above 900 mAh g^{-1}. This can be attributed to its better crystallinity and highly porous structure, which improves the structural stability of the material, increases the active area in contact with the electrolyte and provides sufficient space for the volume change of the lithium storage process. The above results show that the zinc ferrite material obtained by the simple and efficient combustion method is a promising anode material for lithium-ion batteries. The calcination temperature can influence the morphology and crystal structure, thereby influencing the electrochemical performance.

ACKNOWLEDGMENTS
The project was supported by Science and Technology Program of Education Department of Jiangxi Province in China (No. GJJ180464) and Scientific Research Foundation of JiangXi University of Science and Technology (jxxjbs17057), National Natural Science Foundation of China (No. 51564021, No. 21965017).

References

1. H. Shang, Z. C. Zuo, L. Li, F. Wang, H. B. Liu, Y. J. Li and Y. L. Li, *Angew. Chem. Int. Edit.*, 57 (2018) 774.
2. H. D. Liu, J. M. Huang, C. J. Xiang, J. Liu and X. L. Li, *J. Mater. Sci-Mater. El.*, 24 (2013) 3640.
3. S. B. Xia, F. S. Li, F. X. Chen and H. Guo, *J. Alloys Compd.*, 731 (2018) 428.
4. L. Ma, X. Y. Pei, D. C. Mo, Y. Heng, S. S. Lyu and Y. X. Fu, *J. Mater. Sci-Mater. El.*, 30 (2019) 1.
5. J. M. Liu, R. X. Wang, X. C. Zhong, K. Yan, Y. H. Li and Z. F. Xu, *Int. J. Electrochem. sc.*, 14 (2019) 1725.
6. X. M. Lou, J. L. Huang, T. P. Li, H. X. Hu, B. N. Hu and Y. X. Zhang, *J. Mater. Sci-Mater. El.*, 25 (2014) 1193.
7. S. B. Xia, S. W. Yu, L. F. Yao, F. S. Li, X. Li, F. X. Cheng, X. Shen, C. K. Sun, H. Guo and J. J. Liu, *Electrochim. Acta*, 296 (2019) 746.
8. C. S. Yan, G. Chen, X. Zhou, J. X. Sun and C. D. Lv, *Adv. Funct. Mater.*, 26 (2019) 1428.
9. S. H. Wu, G. L. Fu, W. Q. Lv, J. K. Wei, W. J. Chen, H. Q. Yi, M. Gu, X. D. Bai, L. Zhu, C. Tan, Y. C. Liang, G. L. Zhu, J. R. He, X. Q. Wang, K. H. L. Zhang, J. Xiong and W. D. He, *Small*, 14 (2019) 1702667.
10. D. Y. Feng, H. Yang and X. Z. Guo, *Chem. Eng. J.*, 355 (2019) 687.
11. Y. Zhao, X. F. Li, B. Yan, D. B. Xiong, D. J. Li, S. Lawes and X. L. Sun, *Adv. Energy Mater.*, 6 (2016) 1502175.
12. J. J. Ma, M. S. Zhan and K. Wang, *Acs Appl. Mater. Inter.*, 7 (2014) 563.
13. Z. Xing, Z. C. Ju, J. Yang, H. Y. Xu and T. Y. Qian, *Electrochim. Acta*, 102 (2013) 51.
14. H. Xia, Y. Y. Qian, Y. S. Fu and X. Wang, *Solid State Sci.*, 17 (2013) 67.
15. X. B. Zhong, Z. Z. Yang, H. Y. Wang, L. Lu, B. Jin, M. Zha and Q. C. Jiang, *J. Power Sources*, 306 (2016) 718.
16. F. Zou, X. L. Hu, Z. Li, L. Qie, C. C. Hu, R. Zeng, Y. Jiang and Y. H. Huang, *Adv. Mater.*, 26 (2014) 6622.
17. J. F. Wu, Y. H. Song, R. H. Zhou, S. H. Chen, L. Zuo, H. Q. Hou and L. Wang, *J. Mater. Chem. A*, 3 (2015) 7793.
18. L. M. Yao, X. H. Hou, S. J. Hu, Q. Ru, X. Q. Tang, L. Z. Zhao and D. W. Sun, *J. Solid State Electrochem.*, 17 (2013) 2055.
19. Y. Ding, Y. F. Yang and H. X. Shao, *Electrochim. Acta*, 56 (2011) 9433.
20. Z. S. Wu, W. C. Ren, L. Wen, L. B. Gao, J. P. Zhao, Z. P. Chen, G. M. Zhou, F. Li and H. M. Cheng, *ACS Nano*, 4 (2010) 3187.
21. J. X. Wang, Q. B. Zhang, X. H. Li, B. Zhang, L. Q. Mai and K. L. Zhang, *Nano Energy*, 12 (2015) 437.
22. N. Sivakumar, S. R. P. Gnanakan, K. Karthikeyan, S. Amaresh, W. S. Yoon, G. J. Park and Y. S. Lee, *J. Alloys Compd.*, 509 (2011) 7038.
23. Y. Pan, Y. Zhang, X. Wei, C. Yuan, J. Yin, D. Cao and G. Wang, *Electrochim. Acta*, 109 (2013) 89.
24. J. Mao, X. Hou, X. Wang, S. Hu and L. Xiang, *Mater. Lett.* 161 (2015), 652.
25. S. Peng, L. Li and M. Srinivasan, *J. Energy. Chem.*, 23 (2014) 301.
26. C. Wang, Y. Li, Y. Ruan, J. Jiang and Q.H. Wu, *Mater. Energy Today*, 3 (2017) 1
27. X. Wu, W. Wu, Y. Li and F. LiandS. Liao, *Mater. Lett.*, 138 (2015) 192.
28. X. Zhang, T. Chen, D. Yan, W. Qin, B. Hu, Z. Sun and L. Pan, *Electrochim. Acta*, 180 (2015) 616.
29. P. Kollu, P.R. Kumar, C. Santosh, D.K. Kim and A.N. Grace, *RSC Adv.*, 5 (2015) 63304.

© 2020 The Authors. Published by ESG (www.electrochemsci.org). This article is an open access article distributed under the terms and conditions of the Creative Commons Attribution license (http://creativecommons.org/licenses/by/4.0/).